33RD CONGRESS
OF THE INTERNATIONAL COUNCIL
OF THE AERONAUTICAL SCIENCES
STOCKHOLM, SWEDEN, 4-9 SEPTEMBER, 2022

ICAS 2022 SWEDEN

AEROELASTIC MODELING, LOADS ANALYSIS AND STRUCTURAL DESIGN OF A FIGHTER AIRCRAFT

Arne Voß[1], Thomas Klimmek[1]

[1]DLR - German Aerospace Center, Institute of Aeroelasticity, Göttingen, Germany, arne.voss@dlr.de

Abstract

The DLR Future Fighter Demonstrator (FFD) is a highly agile, two-seated aircraft with twin-engines with reheat and a design flight speed extending into the supersonic regime up to Ma=2.0. Based on a given conceptual design, this work focuses on the aeroelastic modeling, including structures, masses and aerodynamics. With these models, a comprehensive loads analysis with 688 maneuver load cases, covering the whole flight envelope, is performed. Based on the resulting section and nodal loads, the structural model is subject to a structural optimization resulting in a preliminary, total primary structural mass of ~3.3t. To confirm the results, the aerodynamic panel methods (VLM and ZONA51) are compared to higher fidelity results obtained from CFD, showing a moderate agreement in terms of surface pressure distribution.

Keywords: Aeroelasticity, maneuver loads, military aircraft, structural optimization, supersonic panel methods

1. Introduction and Motivation

1.1. Objectives

Within a DLR-internal project, a conceptual design of a fighter aircraft is developed. In this work, we focus on the aeroelastic modeling and the loads analysis followed by a structural sizing. Because the design flight envelope extends into the supersonic range, special attention needs to be put on the aerodynamic methods. For the subsonic load cases, the vortex lattice method is used while for the load cases with Ma > 1.0, a supersonic aerodynamic panel method (ZONA51) is employed. Both

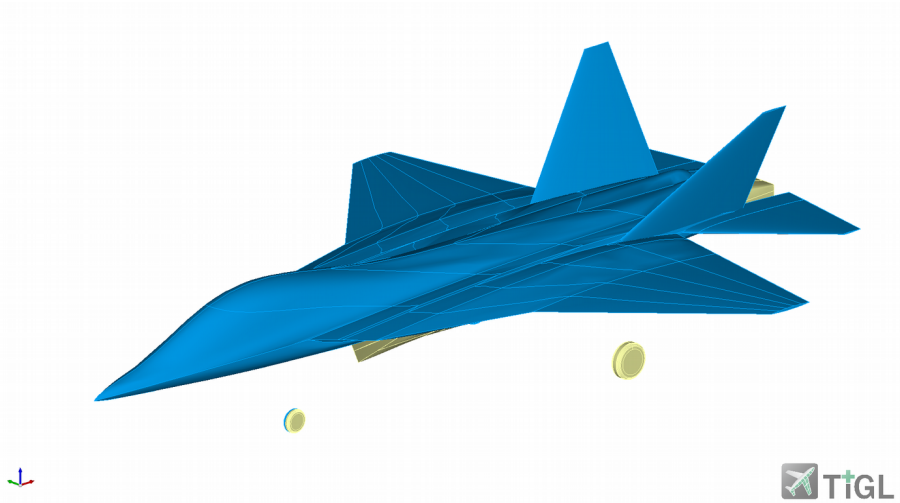

Figure 1 - The DLR Future Fighter Demonstrator (FFD), CPACS file visualized in the TiGL Viewer

Maximum speed	VC = Ma 2.0 at 36,000 - 50,000 ft VD = Ma 2.3 at 36,000 - 50,000 ft
Maximum altitude	50,000 ft
Mission radius	550 - 700 NM
Mass	30.0 – 36.0 t maximum take-off mass (MTOM)
Payload	air 2 air mission: 1820 kg (internal) optional: 8000 kg (internal + external)
Agility	Load factor N_z = -3.0 … +9.0 with basic flight design mass (BFDM)
Longitudinal Stability	Subsonic: unstable, supersonic: stable
Control surfaces	All-movable horizontal tail planes (pitch and roll) 2 vertical tail planes with rudder (yaw)

Table 1 - Overview of DLR Future Fighter Demonstrator (FFD) key design parameters

aerodynamic methods are compared to higher fidelity results obtained from CFD to assessment their validity and/or possible shortfalls.

1.2. The DLR Future Fighter Demonstrator

The DLR Future Fighter Demonstrator (FFD) is a highly agile, two-seated aircraft with twin-engines with reheat and a targeted maximum take-off mass between 30.0 – 36.0 t. An overview of the key parameters is given in Table 1. Within the project, the DLR Institute of System Architectures in Aeronautics has taken the task to devise a conceptual design that fulfills the top level aircraft requirements (TLARs) which were defined before in a project-internal specification document. A special software and a knowledge based approach is used that relies on empirical correlations from a multitude of disciplines. They are combined with an automated constraint and mission capability analysis. More details on that approach are given by Mancini et al. [18]. The resulting conceptual design is then enhanced with a more detailed aerodynamic shape [34] in a manual step by the DLR Institute of Aerodynamics and Flow Technology. The resulting geometry of the FFD is shown in Figure 1. In parallel, an engine is designed by the DLR Institute of Propulsion Technology**.** To enable the exchange of information within the project, the Common Parametric Aircraft Configuration Schema (CPACS) [1] is used.

1.3. Literature Review

For civil configurations, a lot of knowledge on loads analysis and structural sizing exists and, correspondingly, a significant number of publications are available. Some selected DLR publications are by Schulze et al. [28] with a focus on an optimal load adaptive wing and by Klimmek et al. [14] with a focus on the integration into a multidisciplinary optimization chain. Handojo [9] investigated the influence of loads alleviation and fatigue and Sinha et al. [31] concentrated on the composite material modeling. Unconventional configurations, such as flying wings, are studied by Voß [37], Hecken et al. [10] investigated on cargo drones and Voß et al. [39,40] performed the loads analysis for a high altitude, long endurance configuration. Most aircraft companies have developed their own methods and tools, but literature is rarely available. Lockheed developed the L-1011 TriStar using computational methods for loads analysis, as reported by Stauffer et al. [32,33]. Next to Lockheed, work was also done at Boeing, e.g. by D'Vari and Baker [6] presenting an aeroelastic integrated loads subsystem. A framework used at Airbus and DLR is VarLoads, literature can be found by Kier et al.

[11,12] or Scharpenberg et al. [27]. The software used in this work is the Loads Kernel, which is a DLR in-house tool. The theoretical background is documented in [36,38].

Considering that most of the development work of military configurations is confidential, a surprisingly large number of contributions with in-depth information on loads requirements can be found in two comprehensive resources [20,21] published by the NATO Research and Technology Organization and the NATO Advisory Group for Aerospace Research and Development (AGARD). For example, Petiau [23] gives some background on the philosophy of design loads at Dassault (w.r.t. Dassault's Mirage and Rafale). Neubauer and Günther [22] give a general overview on the strategy for loads analyses at Airbus Defense and Space (w.r.t. Tornado and Eurofighter). Watson [41], from British Aerospace, gives details on the structural design criteria with a detailed discussion on dimensioning load cases (w.r.t. Eurofighter). Luber et al. [17] discuss the impact of different dynamic loads on an aircraft design and give details on the calculation procedures (w.r.t. Eurofighter). Molkenthin [19] explains how Airbus tries to develop so-called standardized maneuvers, which can be derived from actual operational maneuvers that are practiced by pilots to achieve a specific motion of the aircraft. From these standardized maneuvers, operational flight loads can be derived as shown by Struck and Perron [35]. The literature mentioned above gives a deep insight into industrial practice and shows that the loads analysis is an essential part in the course of the development process of a new aircraft.

2. Aeroelastic Modeling

2.1. Parametric Geometrical Modeling

For the set-up of the aeroelastic simulation models, namely the structural model, the mass models for the primary structure and the fuel, the aerodynamic model, and the aero-structural coupling model, the parametric model generator ModGen [13] is used, which is developed at the DLR Institute of Aeroelasticity. For this work, various geometry-related features are developed and implemented into ModGen with the aim to derive the basic outer geometry directly from the CPACS dataset, which is set-up during the conceptual design of the DLR Future Fighter Demonstrator (FFD). Note that in previous ModGen applications, the outer geometry was defined by internal ModGen specific parameters and input conventions.

To deal with the outer geometry defined by CPACS for the FFD configuration, the parametric geometrical functions (mainly B spline functions representing curves and surfaces), are set-up within ModGen, similar to DLR's TiGL functions [30]. This concept ensures that the outer geometry is as close as possible to the geometry defined by the CPACS dataset. Then, ModGen's internal geometry processing capabilities are applied for the set-up of geometry models for the primary structure parts like spars and ribs, see Section 2.2, and to create an outer hull for CFD mesh generation, see Section 2.4. For a smooth wing-fuselage geometry, the wing and the fuselage are defined in CPACS as one wing running from left to right and are partitioned into segments. To ensure at least C2 and in part C0 continuity between the segments, so-called guiding curves are defined for the complete wing and fuselage geometry, which are shown in Figure 2. The use of guiding curves leads to a segment wise definition of the outer geometry with so-called Gordon surfaces [15]. Gordon surfaces are created by interpolating a proper curve network, where the intersection points between the curves are known. Gordon surfaces are different from tensor product splines, that are a collection of various polynomial surfaces which are connected with distinct continuity.

The blending surface interpolates the $n \times m$ curve network $f_i(u)$ and $g_j(v)$ for the parametric directions u and v and the blending functions $\Psi_i(v)$ and $\Phi_j(u)$:

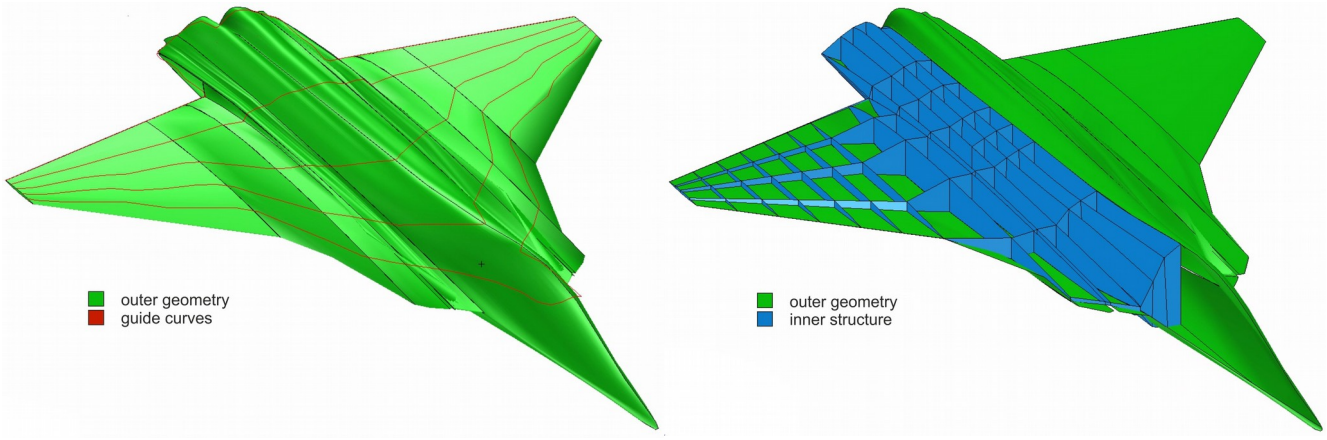

Figure 2 - Processing of the outer aircraft geometry using guiding curves (left) and set-up of the internal geometrical layout for structural modeling (right)

$$s\left(u,v\right)=\sum_{i=1}^{n}f_i\left(u\right)\Psi_i\left(v\right)+\sum_{j=1}^{m}g_j\left(v\right)\Phi_j\left(u\right)-\sum_{i=1}^{n}\sum_{j=1}^{m}p_{i,j}\Phi_j\left(u\right)\Psi_i\left(v\right) \tag{2.1}$$

with the intersection points $p_{i,j}$ between n curves f and the m curves g. Rewriting eq. (2.1) leads to

$$s\left(u,v\right)=s_f\left(u,v\right)+s_g\left(u,v\right)-t\left(u,v\right) \tag{2.2}$$

where $s_f\left(u,v\right)$ and $s_g\left(u,v\right)$ represent the individual spline interpolation for the curve families f and g. The surface $t\left(u,v\right)$ is a so-called tensor product surface using the intersection points $p_{i,j}$ and the blending functions $\Psi_i\left(v\right)$ and $\Phi_j\left(u\right)$.

In order to make the formula for s applicable for the profile curves and the guide curves of the FFD configuration, which represent the two curve families f and g, several steps to harmonize the parameterization of the curves have to be done. The potential different parametrization of even the curves is basically rooted in the fact that each curve is individually defined to fit best for the target geometry. As far as B-splines were chosen for the parametric curves and surfaces, the curves within its family have to have the same knot set and order and for the superposition together with the blending functions $\Psi_i\left(v\right)$ and $\Phi_j\left(u\right)$, the surfaces $s_f\left(u,v\right)$, $s_g\left(u,v\right)$ and $t\left(u,v\right)$ have to be compatible (same knot set and same order of u and v parametric directions) as well, such that all three surfaces can be superposed to $s\left(u,v\right)$. A formal and exact harmonization would lead to a surface definition with a massive number of parameters and high order. Therefore, in a first step, each surface $s_f\left(u,v\right)$, $s_g\left(u,v\right)$ and $t\left(u,v\right)$ is set-up individually after harmonizing the curves. Then, in the second step, the surfaces are re-parametrized by extracting proper numbers of curves and splining them again to obtain $\widetilde{s}_f\left(u,v\right)$, $\widetilde{s}_g\left(u,v\right)$ and $\widetilde{t}\left(u,v\right)$. Now, the number $\widetilde{n}$ and $\widetilde{m}$ of the curves per surface and the knot set and order of the curves are defined in a coordinated way such that the superposition yields $\widetilde{s}\left(u,v\right)$.

For the definition of the internal load carrying structure, like spars and ribs, a classical definition conventions with respect for the number, position, and orientation, is applied, resulting in a internal structural layout shown in Figure 2 on the right in blue color. Together with the upper and lower skin, this internal geometrical layout provides the baseline for the set-up of the grids and finite element models, which are described in the following Sections.

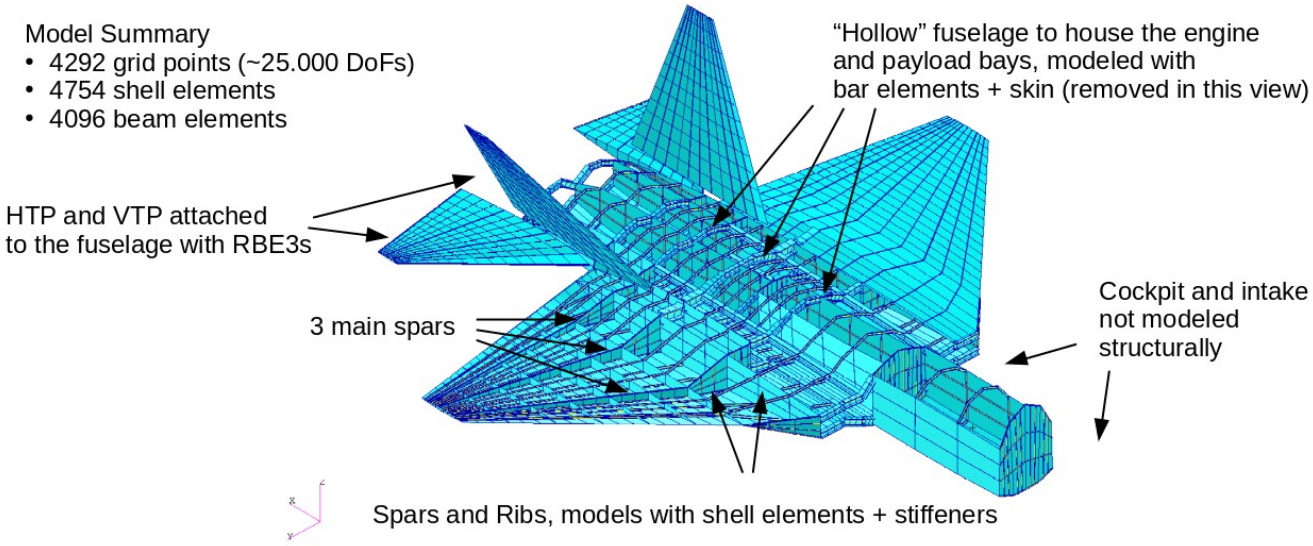

Figure 3 - Structural modeling using finite elements

2.2. Structural Model

The first aim of the structural model is to adequately represent the overall structural dynamic characteristics of the aircraft (e.g. wing bending and twist), which are important for aeroelastic analyses. Second, the model shall provide a baseline for the structural sizing, which is described in Section 4. Therefore, all primary structural elements, including the spars, ribs, upper and lower skin, are modeled using shell elements (CQUAD4, PSHELL and MAT1) and are completed by spar caps, stiffeners and stringers, using beam elements, to avoid local buckling and to provide a more realistic structure. For the wing, a structural layout with three main spars and multiple ribs, orientated in flow direction, is devised, see Figure 3. From an ideal structure point of view, the main spars would continue up to the center line of the aircraft, providing a good load path and high second area moments to take the wing root bending moments. However, the majority of the available space in the fuselage region is taken up by the twin-engines and the air intakes. Most of the remaining space is taken by the weapon and landing gear bays as well as by fuel tanks. Thus, the main spars are discontinued and the “hollow” fuselage region is bridged by standard I-beam (alternative names: double T- or H-beam) elements (CBAR, PBARL and MAT1) located on the top and bottom, providing sufficient space for the engines, air intake, etc. in between. Note that the beam elements are only representative and should be replaced by a more detailed structure in future design phases. Because the beam's cross sections are included in the sizing, see Section 4, they provide a good estimate in terms of required cross section and second area moment. Similar to the wing, the horizontal and the vertical tail are modeled and attached to the rear fuselage using rigid body elements (RBE3). Not included in the structural model are the air intakes and the cockpit. The rational behind this decision is that although both components are large, they don't belong to the primary, load-carrying structure and their influence on the overall structural dynamic behavior of the aircraft is neglected though their mass and moment of inertia is considered. The resulting MSC.Nastran finite elements model is shown in Figure 3, has a size of ~25.000 degrees of freedom (DoF) and includes 4292 grid points, 4754 shell elements and 4096 beam elements.

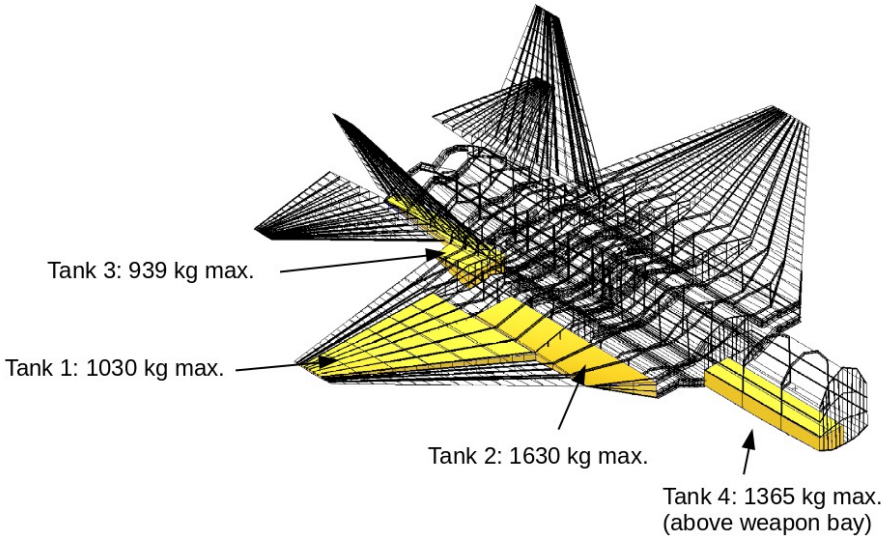

Figure 4 - Fuel modeling using volume elements to estimate mass and inertia properties

2.3. Mass Model

For loads analysis it is important that the mass model is as complete as possible and that the masses are distributed over the aircraft at their actual location, because both has a significant impact on the section loads. The mass model includes the structural masses, system masses, fuel masses and payload. The structural masses are derived from the skin thickness and/or the cross section of the beam elements combined with the material density. Note that when the material thickness changes during the sizing, this has an influence on the structural weight. The structural masses are completed by mass estimates for the components not included in the structural model (e.g. air intakes and cockpit). For the aircraft systems, empirical mass estimates are available from the conceptual design. Also, a total of 9909 kg of fuel is estimated, which is distributed over four fuel tanks per side as shown in Figure 4. The fuel is then modeled with volume elements and MSC.Nastran is used to calculate both mass and inertia properties. Finally, a design payload of 1820 kg for an air to air missions is taken into account, distributed over three weapon bays.

To combine the structural stiffness and mass model, an approach with one condensed mass per sub-section is used. One sub-section is described for example by two ribs, two spars and the surrounding skins. The individual masses are condensed at the center of each sub-section using a nearest-neighbor approach, the inertia properties are maintained. The center grid points are connected to the corner points of each sub-section using rigid body elements, so that the inertia forces will be introduced into the structure smoothly without creating undesired local stress peaks.

Different combinations of fuel and payload masses are considered using four mass configurations summarized in Table 2 and shown in Figure 5. The configurations M1 to M4 are selected in such a way that they roughly represent the different mass cases that occur during a mission of the aircraft, ranging from the heaviest mass case M1 at take-off to the lightest mass case M4 just before landing. Mass case M2 corresponds to the basic flight design mass (BFDM) where the aircraft is required to achieve its full performance.

Mass case	Fuel	Payload	Mass
M1 (MTOM)	100%	Yes	26.2t
M2 (BFDM)	70%	Yes	23.2t
M3	70%	No	21.4t
M4 (OEM)	0%	No	14.5t

Table 2 - Overview of mass configurations

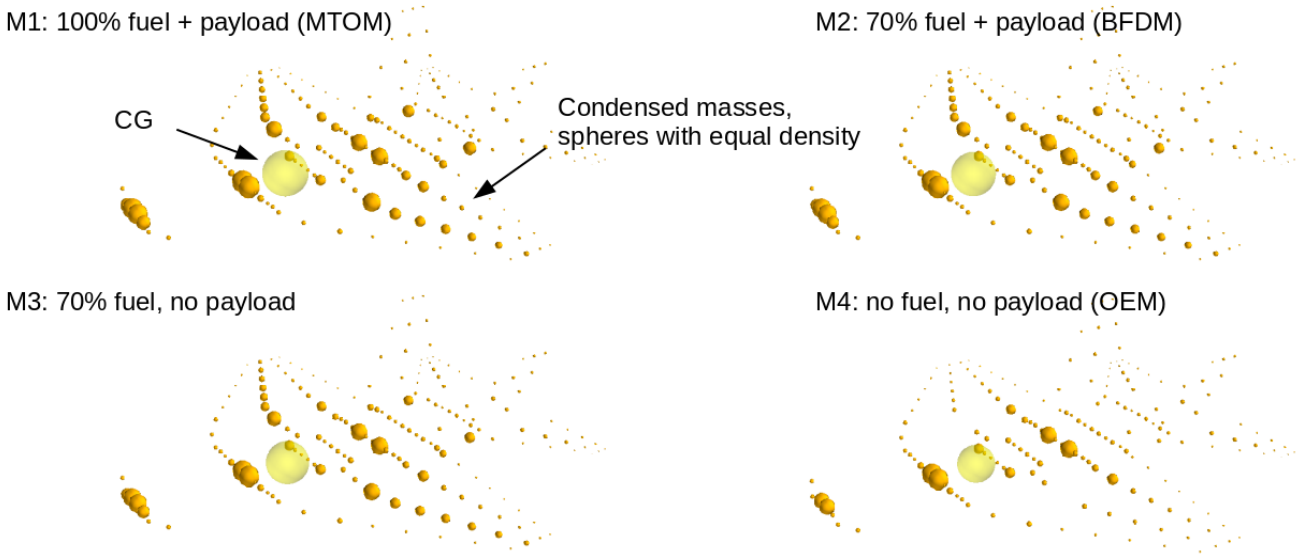

Figure 5 - Mass modeling with condensed masses and four mass cases

Note that on the aerodynamic side, there is a significant shift of the aerodynamic center (AC) between the subsonic and the supersonic regime (compare with flat plate: subsonic AC at ~25%, supersonic AC at ~50%). Therefore, the initial concept considered a longitudinal instability of 10% MAC in the subsonic range to avoid a too high longitudinal stability in the supersonic range. Because this leads to high angles of attack for the HTP, this criterion was relaxed for this work to a subsonic longitudinal instability of ~2-3%, accepting an increased stability for the supersonic range, which was achieved by shifting some masses within the fuselage towards the front.

2.4. Aerodynamic Model

To obtain aerodynamic pressure distributions, the vortex lattice method (VLM) [36] is used for the subsonic regime and the ZONA51 method [4,16] for the supersonic regime. For both methods, the lifting surfaces are discretized using a panel mesh shown in Figure 6. The mesh consists of 1112 panels and four control surfaces. The left and right horizontal tail planes (HTP) are all-movable and are used for both pitch and roll control while the left and right vertical tail planes (VTP) have a conventional rudder. Although the aerodynamic methods consider the lifting surfaces as flat plates, it is possible to add a correction for airfoil camber and wing twist, which is indicated by the color in Figure 6. Note that currently a (preliminary) symmetric airfoil is used for the wings, so the main influence of this correction can be seen in the fuselage region.

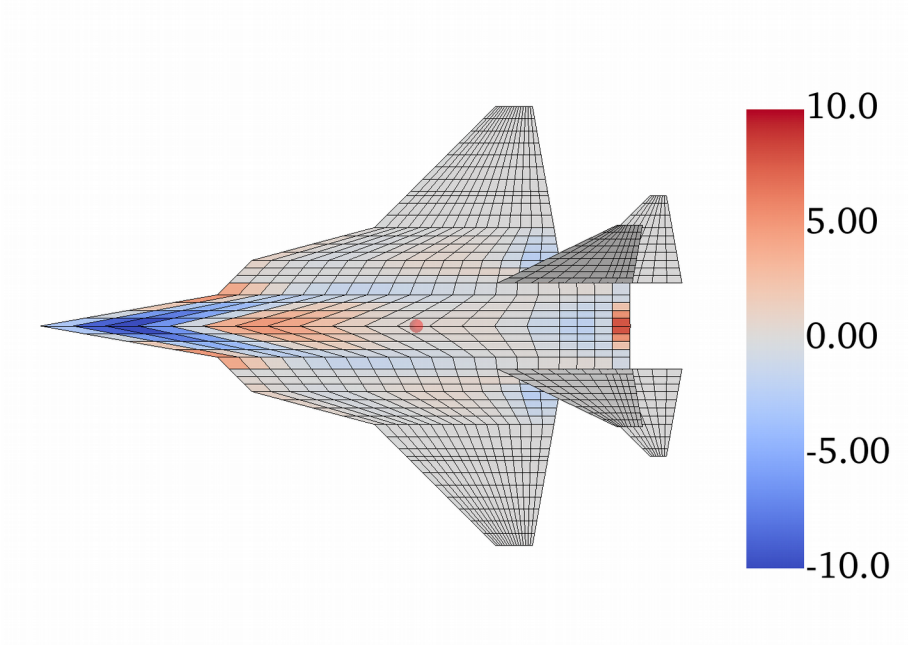

Figure 6 - Aerodynamic mesh for VLM & ZONA51 incl. correction for camber and twist (indicated by color)

Following Watson [41], linear aerodynamics are adequate for calculating design loads, as the highest loads typically arise at high-speed conditions where the aerodynamics remain within their linear regime. To assessment their validity and/or possible shortfalls, both aerodynamic panel methods are compared with higher fidelity results obtained from CFD in Section 5. Considering that for loads analyses, capturing all major physical effects adequately (but not precisely or to the last detail as an aerodynamic specialist would prefer) is important, the authors believe that the Euler equations are a reasonable choice when comparing computational cost and precision of the results. From Probert's overview on the wing design of combat aircraft [26], it can be concluded that much of the aerodynamic design work for the Tornado and the Eurofighter was performed using Euler codes. In this work, the DLR Tau [29] code and the SU2 [7] code are used. The underlying aerodynamic mesh is generated based on the outer geometry generated with ModGen, which in turn relies on a CPACS files as described in Section 2.1. The HTP and VTP geometry are blended with the main aircraft using Siemens Simcenter 3D. The meshing is performed using Centaur and results in a surface mesh with

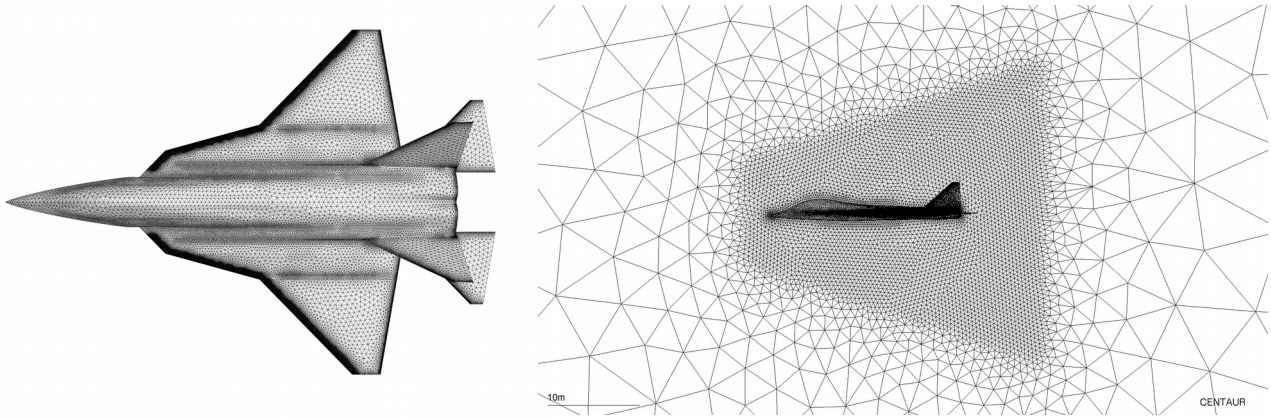

Figure 7 - Aerodynamic mesh for CFD solution

~206k triangles as shown in Figure 7 on the left. Because no boundary layer is required for Euler solutions, tetrahedrons can be used directly to fill a spherical control volume. To better resolve vortices, which are expected already at low angles of attack, the volume mesh is refined in proximity to the aircraft using a conical frustum, visualized in Figure 7 on the right. This results in a mesh with a total number of 4.4M volume cells. Note that the same aerodynamic mesh is used for both flow solvers, the only difference is the conversion into the native mesh format of each CFD solver.

3. Loads Analysis

3.1. Load Case Selection

There are a large variety of steady and dynamic load cases that have an influence on the design of an aircraft, e.g. dynamic gust encounter, buffet loads on the rear of the aircraft, gunfire loads at attachment points, so-called hammershock loads at the air intake, bird strike, jettison, landing loads, ground loads, etc. (compare with Luber et al. [17]). Because each type of load case requires a special analysis and in several cases also data from experimental measurements and because most load cases are only relevant for a specific part of the aircraft, taking everything into account is not feasible for an early preliminary design stage. Based on their experience with civil transport aircraft, the authors of this work assume that for the sizing of the primary aircraft structure, both maneuver and gust loads are potential driving factors. More elaborate load analysis may be added at later stage during the design process.

As a simplified means to estimate gust loads, the Pratt formula [24,25] allows to translate a gust encounter into an equivalent load factor N_z. For the FFD configuration, the highest Pratt load factor obtained was $N_z \leq 3.0$, which is much lower than the maximum load factor $N_{\mathrm{z,max}} = 9.0$ from the maneuver load cases. Knowing that the Pratt formula is designed for classical transport and not for fighter aircraft, the authors still believe that the results are at least representative and, consequently, gust loads can be ruled out for the sizing of the primary, load-carrying structure of this aircraft. Note that a gust encounter could still be important, for example a short gust might lead to high local accelerations at the wing tip, which might be dimensioning for under-wing attachment points, see Luber et al. [17].

Concerning maneuver load cases, time domain simulations with cockpit control displacements as given e.g. in MIL-A-8861B [43] are not feasible during the preliminary design phase, because this would involve an electronic flight control system (EFCS) which is not yet available at this stage of the design process. Also, because no measurements or flight test data are available, operational flight loads are neither an option. Thus, a number of representative design load cases are derived from the aircraft requirements. This is a pragmatic approach for the preliminary design and is also used e.g. at Dassault as stated by Petiau [23] and for the Eurofighter as explained by Watson [41]. The task of the EFCS is then to ensure that the aircraft stays within the boundaries set by the design load cases. Should more detailed knowledge and/or the flight test reveal the assumptions were too conservative, the additional margin can be used by the EFCS for the benefit of better flying and handling qualities.

The flight envelope of military aircraft shown in Figure 8 and defined in MIL-A-8860B [42] and MIL-A-8861B [43] follows a similar approach compared to the flight envelope of civil aircraft defined for example in CS-25 [8]. In this work, the military flight speeds V are indicated with a subscript and the civil flight speeds with a capital character. For example, the level flight maximum speed V_H corresponds to the design cruising speed VC, the limit speed V_L corresponds to the design dive speed VD and the minimum speed V_e at which the design limit load factor can be attained corresponds to the design maneuvering speed VA. The left side of the flight envelope is completed by the stall

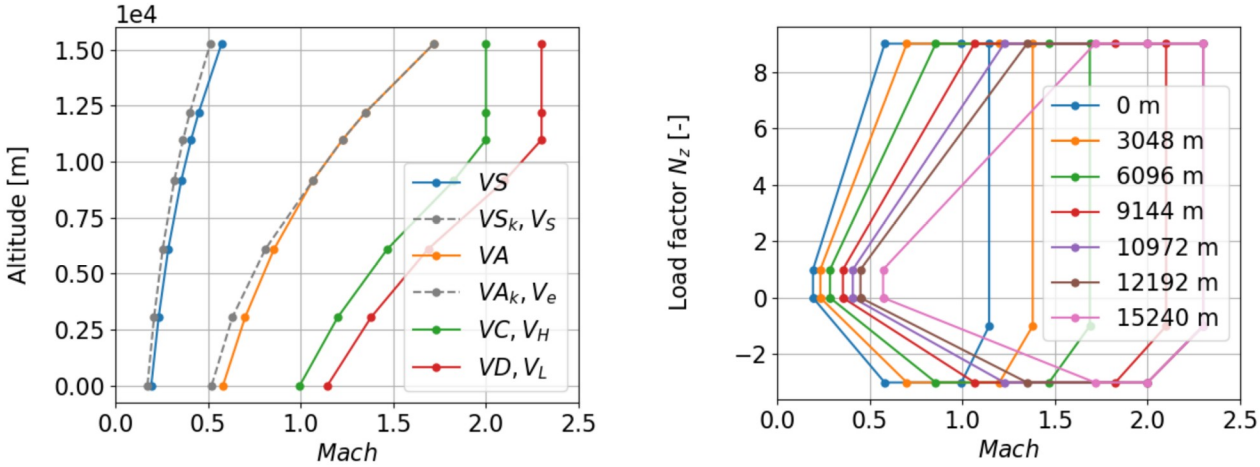

Figure 8 - Proposed design speeds and flight envelope

speeds V_S and VS, which exists in both military and civil specifications. Note that the military specification asks for a reduction of V_S and V_e by a factor $K = 1.0 \ldots 1.25$ for flight speed below Ma=1.0 to account for buffet loads, which are given in Figure 8 by the dashed gray lines. On the aerodynamic side, this would require higher lift coefficients than physically achievable, which is mathematically possible with linear panel methods but can't be achieved using more physical methods such as CFD. Thus, for this work, the authors decided against using the reduction factor K.

The maneuver load cases include pull-up and push-down maneuvers with a load factor $N_z = -3.0 \ldots 9.0$. Both pull-up and push-down maneuvers are combined with maximum elevator commands in opposite direction, which reflects a sudden change of mind by the pilot. Steady roll maneuvers with constant roll rates p as well as accelerated roll maneuvers with $\dot{p}$ in opposite direction are considered for horizontal level flight and in combination with the pull-up and push-down maneuvers. Depending on the flight speed and angle of attack, the roll rate p ranges from $25°/s$ for low speed and high angle of attack to $220°/s$ for higher speed and low angles of attack. In a similar way but with a larger spread, the roll acceleration $\dot{p}$ changes from $\dot{p} = 20°/s^2 \ldots 550°/s^2$. A summary of all parameters is given in Table 3. The maneuver load cases are considered for all flight speeds and at seven different altitudes (every dot in Figure 8 indicates an operational point) because as Neubauer and Günther [22] point out, it is important to consider not only the corner points of the flight envelope but also also operational points within the envelope. The reason is that the interaction of aerodynamics, the flexible structure and control surface deflections is difficult to predict analytically. Also, all four mass configurations M1 to M4 are considered, but not in combination with all maneuver cases becasue for example the maximum load factor $N_{z,\max}$ only has to be reached for M2 (BFDM) but not for M1 (MTOM). As most operational points are above $Ma = 1.0$, this results in a total number of 175 subsonic and 513 supersonic maneuver load cases.

Maneuver load parameters	Value / range
Load factor N_z	$N_z = -3.0 \ldots 9.0$
Roll rate p	$p = \pm 20°/s \cdots \pm 220°/s$
Roll acceleration $\dot{p}$	$\dot{p} = 20°/s^2 \ldots 550°/s^2$
Elevator deflection η	$\eta_{\min,\max} = \pm 15°$

Table 3 - Overview on maneuver load parameters

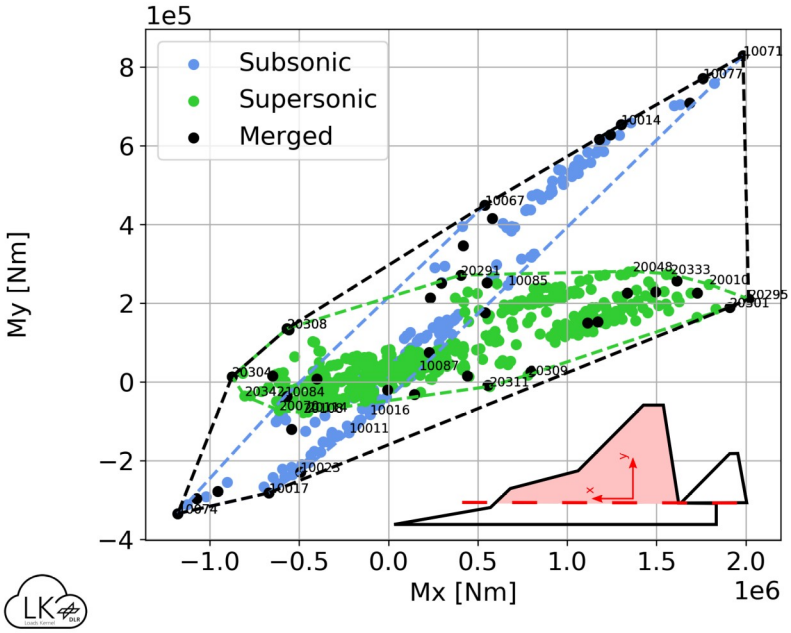

Figure 9 - Bending and torsion moments M_x and M_y at the right wing root

The resulting loads are evaluated in terms of section loads at so-called monitoring stations. Figure 9 shows an example of a two-dimensional envelope of the bending moment M_x and the torsional moment M_y for a monitoring station located at the right wing root. Every dot corresponds to one maneuver load case and the subsonic load cases are plotted in blue while the supersonic cases are plotted in green color. One can clearly see that the maximum bending moment M_x is similar, because maneuvers with high N_z are included for both sub- and supersonic cases. However, the envelope of the supersonic load cases is rotated compared to the subsonic load cases and the torsional moments M_y are much lower for the supersonic cases. This can be explained by the large range of travel of the aerodynamic center, with a location further rearwards for supersonic speeds compared to subsonic speeds. Finally, the convex hull, plotted in black, yields the highest load cases. Some black dots can also be seen within the envelope, which can be explained by the fact that the corresponding load case was identified by a different monitoring station. These load cases are considered as dimensioning load cases for the structural sizing. For this reduced set of load cases, both section and nodal loads are available and can be used for either a manual sizing by the structural department or, in the context of this work, for a structural optimization.

Note that the section load based approach described above has limitations, especially for compact military configurations, because the load paths are not always clear and monitoring stations are difficult to place, especially in the fuselage region. Alternative concept are investigated for example by Bramsiepe et al. [3].

4. Structural Optimization

In this Section, the structural sizing is formulated as a structural optimization problem. The design variables of the FFD are the material thicknesses of the shell elements of the skin, spars and ribs and the cross section of the fuselage beam elements. Note that other parameters, such as stringer size or spacing, remain fixed. The parameters are changed per design field, where one design field is for

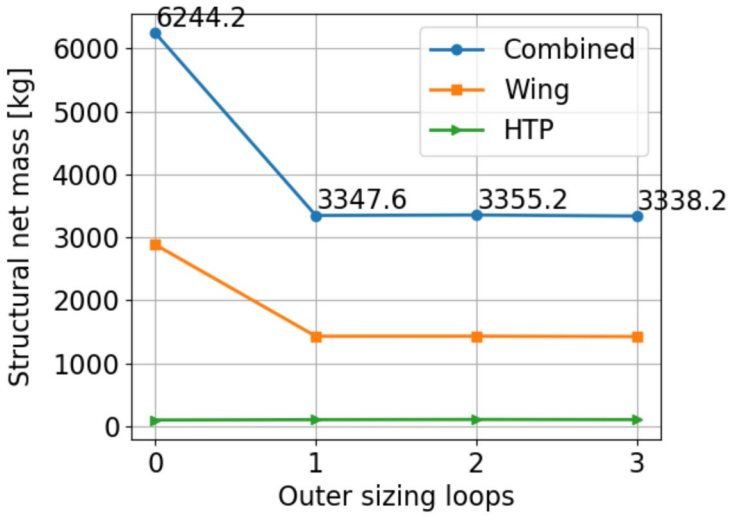

Figure 10 - Mass convergence of the FE model

example the area between two ribs and two spars. The FFD comprises 304 design fields, resulting in 304 design variables $\mathbf{x}$. The objective $f(\mathbf{x})$ is to minimize the structural mass while the constraints $\mathbf{g}$ are satisfied. As constraint, the maximum allowable stress for a 2024 aluminum (3.1354, T3) with $\sigma_{\text{allow}} = \pm 270.0\ \text{MPa}$ is evaluated. Side constraints are the minimum allowable skin thickness $t_{min} = 1.0\ mm$ and the minimum allowable width of the beam profile $w_{min} = 100.0\ mm$ to avoid unrealistic designs. Note that the remaining dimensions of the beam profile are linked and scaled linearly, so that in essence the whole cross section of the beam element is changed. In the previous Section, the loads are calculated as limit loads while the structure is sized with ultimate loads, which equals 1.5 times the limit loads. The physical background is that plastic deformation may occur on a local level beyond limit load but failure of the primary, load carrying structure should not occur up to ultimate load. Some authors, like Watson [41], argue that with a limit load protection included in the EFCS, this factor could be relaxed (e.g. to 1.4) because exceeding limit load is less likely compared with an aircraft where the pilot is responsible for not exceeding the limit loads. In this work, the factor of 1.5 is considered in the allowable stresses.

The loads analysis and the structural optimization form an iterative process, because a change in structural mass influences the loads and vice versa. In this case, mass convergence is achieved quickly after only three loops, as shown in Figure 10, with a final total mass of ~3.3 t. Note that the results are strongly influenced by the selected minimum skin thickness, which is influenced strongly by practical considerations such as impact damage from debris during take-off and landing, so these results mark the lower end of the physical and technical possible.

The resulting material thickness is shown in Figure 11. In many design fields, the minimum allowable skin thickness $t_{min} = 1.0\ mm$ is sufficient, which is indicted by the yellow color. Looking at the lower and upper skin of the wing, a load path where the material thickness is increased is clearly visible between the front and rear spar, indicated by the orange and red colors. This load path is also reflected by the material thickness of the spars, where the middle spar reaches a maximum thickness of about 16.0 mm at the wing root. In a similar way, the material thickness of the HTP is increased between the two spars and the load path is continued into the rear fuselage. Summing up, the optimization results look plausible from an engineering perspective.

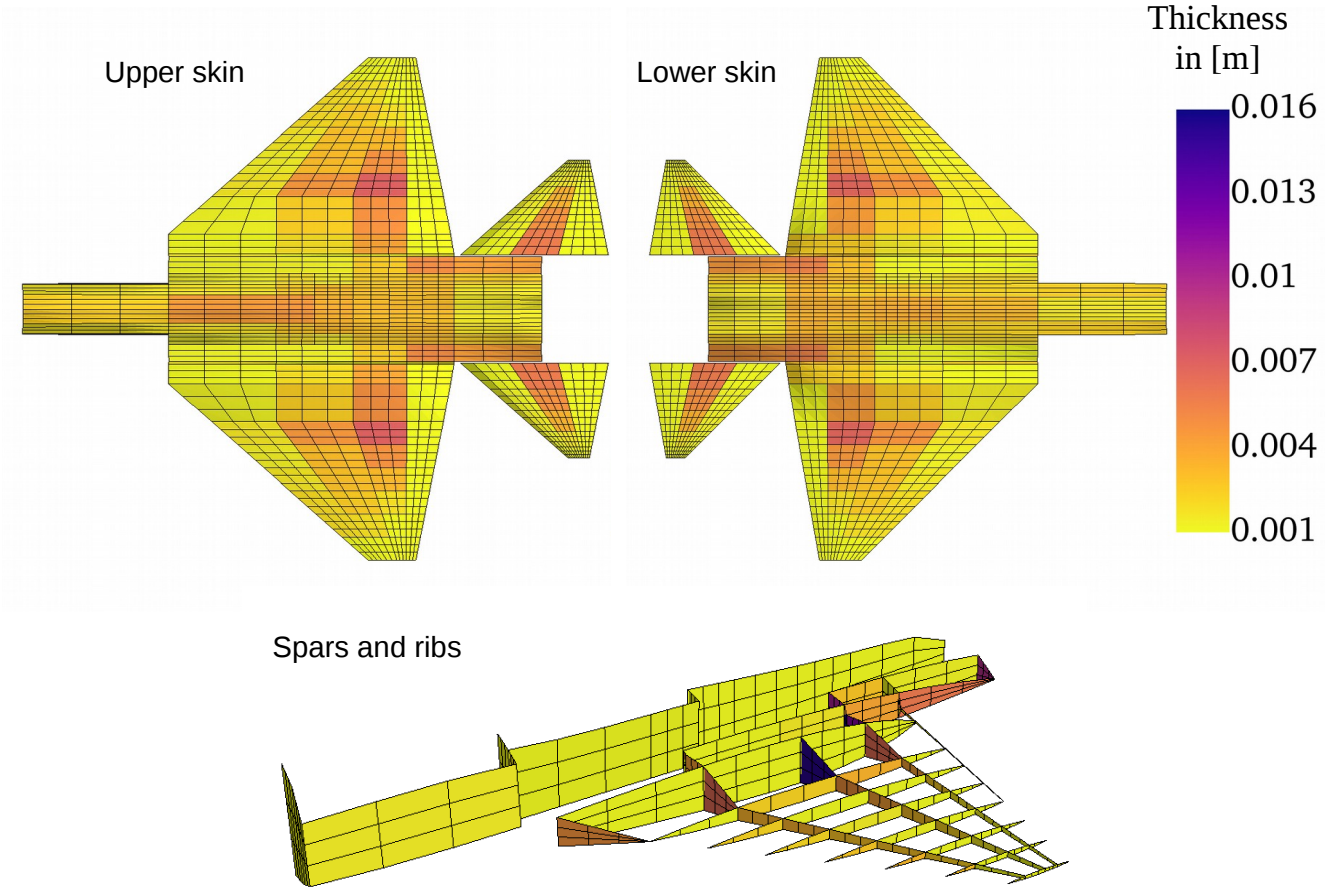

Figure 11 - Resulting material thickness of the shell elements

5. Comparison of Panel Aerodynamics with CFD

The aerodynamic modeling is a great field of uncertainty for two reasons: a) in the subsonic regime, a vortex-dominated flow is expected and b) there is less experience with supersonic panel methods and only few publications are available. To assess the method's validity and/or possible shortfalls, both aerodynamic panel methods (VLM and ZONA51) are compared with higher fidelity results obtained from CFD.

5.1. Subsonic: Tau RANS vs. Tau Euler vs. SU2 Euler

In a first step, three different CFD solutions are compared. The Tau Euler and the SU2 Euler solutions are prepared using the mesh described in Section 2.4 while the Tau RANS solutions [34] are provided by the DLR Institute of Aerodynamics and Flow Technology, for which the authors are very thankful. Figure 12 shows a visualization of the vortices using the Q-criterion [2,5] with iso-surfaces at Q=50 for a representative low-speed operational point at $Ma = 0.4$ and $\alpha = 15.0°$. Two primary vortices can be identified in all three solutions, one starting at the strake and one starting at the leading edge of the main wing. In general, the vortices appear to be slightly stronger in the two Euler solutions compared to the RANS solutions, which is as expected due to the missing viscous dissipation. The surface pressure distributions c_p shown in Figure 13 are very similar in all three solutions, too. The "footprints" of the vortices are visible as suction peaks in green to blue colors.

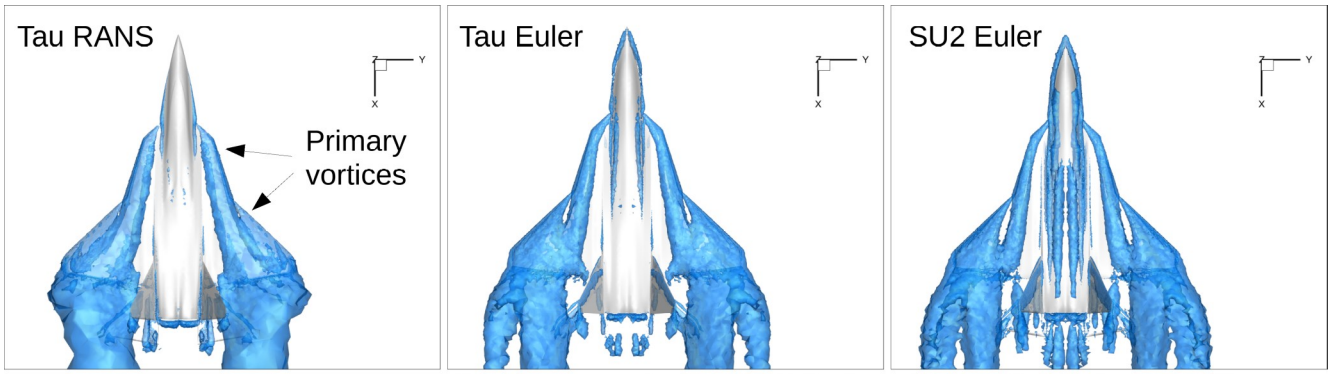

Figure 12 - Visualization of the vortices using the Q-Criterion at $Ma = 0.4$ and $\alpha = 15.0°$

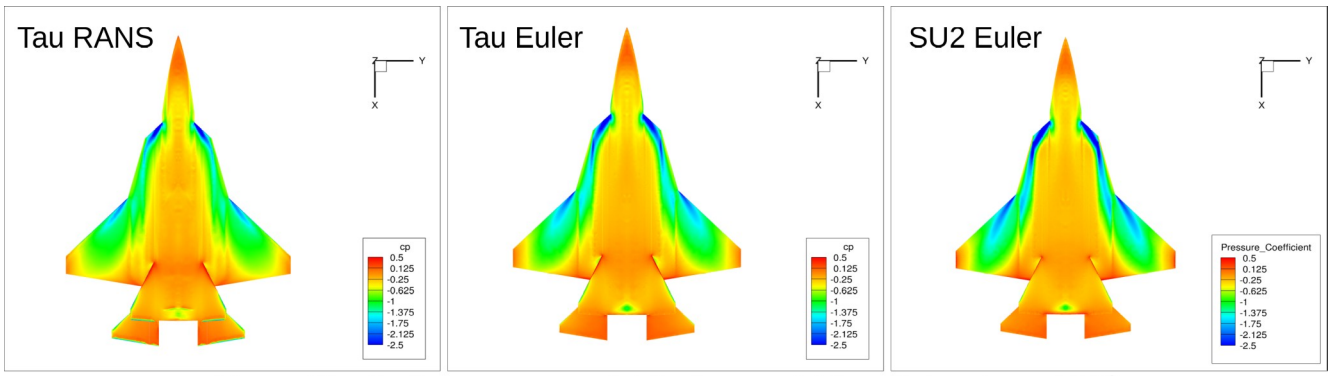

Figure 13 - Surface pressure distribution c_p at $Ma = 0.4$ and $\alpha = 15.0°$

5.2. Subsonic: CFD vs. VLM

In a next step, the CFD solutions are compared to the vortex lattice method (VLM). The VLM [36] is based on a matrix of aerodynamic influence coefficients, the so-called $\mathbf{AIC}$, which only depends on the Mach number Ma, and the geometry of the aircraft. The $\mathbf{AIC}$ matrix then relates an induced downwash $\mathbf{w}_j$ on each aerodynamic panel to a pressure coefficient

$$\mathbf{\Delta c_p^{AIC}} = \mathbf{AIC}(Ma) \cdot \mathbf{w}_j \,. \tag{5.1}$$

This means that the VLM scales purely linear with for example the angle of attack. In addition, because the VLM assumes a flat plate, the pressure coefficient $\mathbf{\Delta c_p^{AIC}}$ yields the pressure difference between upper and lower side. Thus, a comparison with CFD is not straight forward and requires to split the volumetric body of the CFD solution in an upper and lower side (remove the VTP), then to project onto xy-plane and to interpolate the values at the panel centers. Finally, a pressure difference between upper and lower side is calculated with

$$\mathbf{\Delta c}_p^{\text{CFD, interp}} = \mathbf{c}_{p,\text{lower}}^{\text{CFD, interp}} - \mathbf{c}_{p,\text{upper}}^{\text{CFD, interp}} \,. \tag{5.2}$$

Figure 14 shows the pressure coefficient distribution $\mathbf{\Delta c_p}$ for the low-speed operational point at $Ma = 0.4$ and $\alpha = 15.0°$. For the CFD solution, the vortices are clearly visible in the pressure coefficient distribution. However, the VLM solution only shows a suction peak along the leading edge but the vortices are not captured. This is as expected due to the linear approach of the VLM, but leads to a significantly different aerodynamic loading in both span and chord direction.

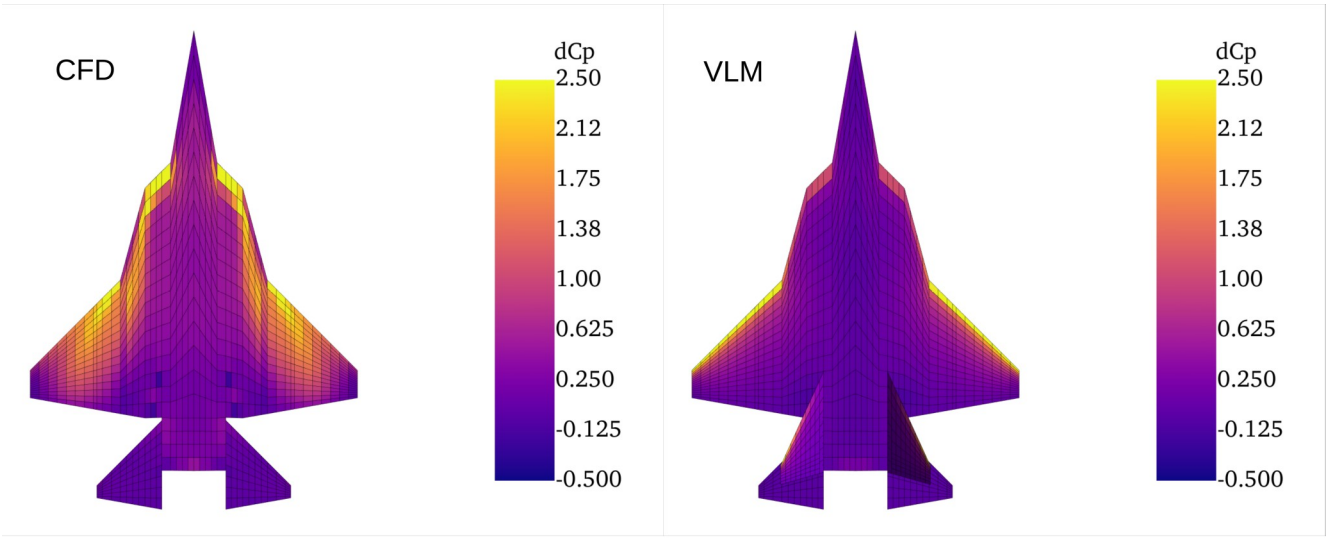

Figure 14 - Pressure coefficient distributions $\mathbf{\Delta c_p}$ at $Ma = 0.4$ and $\alpha = 15.0°$

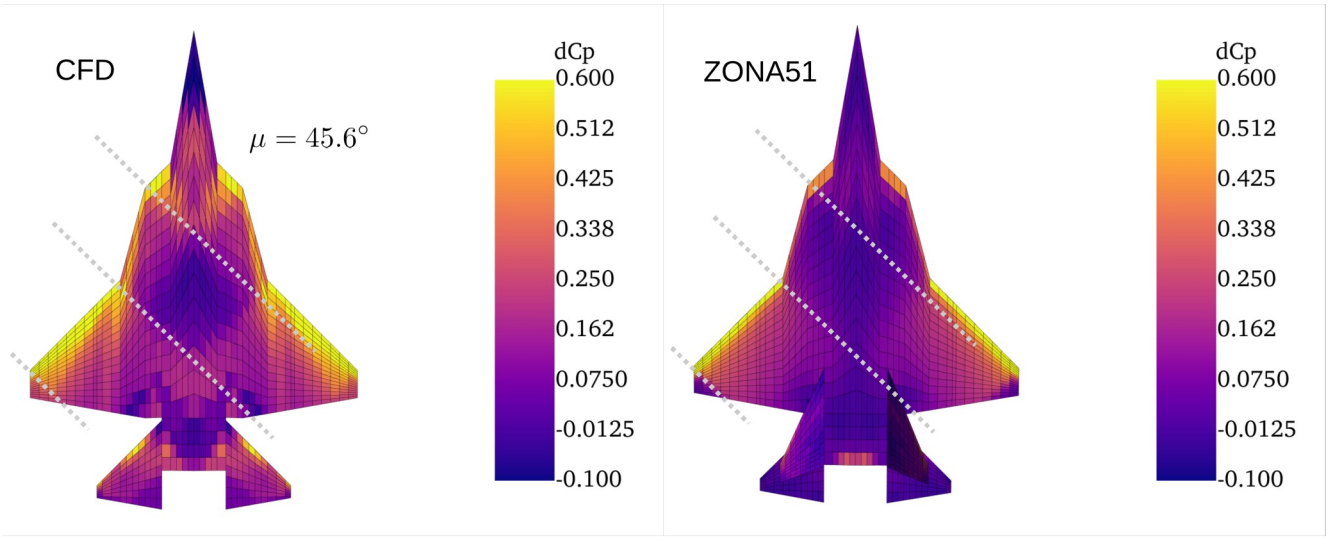

Figure 15 - Pressure coefficient distributions $\mathbf{\Delta c_p}$ at $Ma = 1.4$ and $\alpha = 5.0°$

5.3. Supersonic: CFD vs. ZONA51

Figure 15 shows the pressure coefficient distribution $\mathbf{\Delta c_p}$ for a representative high-speed operational point at $Ma = 1.4$ and $\alpha = 5.0°$. In the supersonic regime, the angle of the compression wave front is given by $\mu = sin^{-1}(1/Ma)$ with $\mu = 45.6°$ for Ma=1.4. The compression shocks result in a jump of the surface pressure distribution. Like in the subsonic regime, vortices are also present in the supersonic regime, making a direct comparison of the pressure distributions between CFD and ZONA51 difficult. Still, compression shocks can be identified in both solutions and at the same locations as indicated by the dashed lines.

5.4. Influence on Maneuver Loads

From the loads analysis perspective, the Euler equations are a reasonable choice for the FFD configuration with respect to computational cost, precision and geometric model requirements. Compared to RANS equations, the Euler results are very similar as shown in Section 5.1 (as well as for all other operational points not included in this paper). The comparison of CFD with the

aerodynamic panel methods shows only a moderate agreement in the sub- and supersonic regime. Still, because section loads are very integral quantities, the overall influence on the preliminary sizing might be less pronounced. This question is subject of future work.

6. Summary and Outlook

Loads and aeroelastic models, comprising structures, masses and aerodynamics, were developed for a future fighter demonstrator (FFD). A comprehensive loads analysis covering the whole flight envelope was performed, with a focus on maneuver loads. Based on an estimate using the Pratt formula, gust loads are expected to have a minor influence only. The resulting loads were then used for a structural optimization, leading to a final total structural mass of ~3.3 t. A comparison of the panel aerodynamics with higher fidelity results obtained from CFD showed a moderate agreement for the overall pressure distribution. The next step is the repetition of the loads analysis and the sizing with CFD maneuver loads. In addition, as the aeroelastic models are now available, further aeroelastic analyses can be performed, for example with respect to control surface effectiveness or flutter.

Contact Author Email Address

arne.voss@dlr.de

Copyright Statement

References

[1] Alder, M., Moerland, E., Jepsen, J., and Nagel, B., “Recent Advances in Establishing a Common Language for Aircraft Design with CPACS,” presented at the Aerospace Europe Conference 2020, Bordeaux, Frankreich, 2020, https://elib.dlr.de/134341/.

[2] Banko, A. J., and Eaton, J. K., “A frame-invariant definition of the Q-criterion,” *Stanford University Center for Turbulence Research Annual Research Briefs*, pp. 181–194, 2019.

[3] Bramsiepe, K., Voß, A., and Herberhold, M., “Aeroelastic load selection based on failure indices on finite element level,” presented at the Deutscher Luft- und Raumfahrtkongress, Bremen, 2021, https://doi.org/10.25967/550237.

[4] Chen, P.-C., and Liu, D. D., “A harmonic gradient method for unsteady supersonic flow calculations,” *Journal of Aircraft*, vol. 22, no. 5, pp. 371–379, 1985, https://doi.org/10.2514/3.45134.

[5] Chong, M. S., Perry, A. E., and Cantwell, B. J., “A general classification of three-dimensional flow fields,” *Physics of Fluids A: Fluid Dynamics*, vol. 2, no. 5, pp. 765–777, May 1990, https://doi.org/10.1063/1.857730.

[6] D’Vari, R., and Baker, M., “Aeroelastic Loads and Sensitivity Analysis for Structural Loads Optimization,” *Journal of Aircraft*, vol. 36, no. 1, pp. 156–166, 1999, https://doi.org/10.2514/2.2421.

[7] Economon, T. D., Palacios, F., Copeland, S. R., Lukaczyk, T. W., and Alonso, J. J., “SU2: An Open-Source Suite for Multiphysics Simulation and Design,” *AIAA Journal*, vol. 54, no. 3, pp. 828–846, März 2016, https://doi.org/10.2514/1.J053813.

[8] European Aviation Safety Agency, ed., *Certification Specifications for Large Aeroplanes CS-25*, Amendment 16. 2015, https://www.easa.europa.eu/certification-specifications/cs-25-large-aeroplanes.
[9] Handojo, V., “Contribution to Load Alleviation in Aircraft Pre-design and Its Influence on Structural Mass and Fatigue,” Dissertation, TU Berlin, Berlin, Germany, 2020.
[10] Hecken, T., Cumnuantip, S., and Klimmek, T., “Structural Design of Heavy-Lift Unmanned Cargo Drones in Low Altitudes,” in *Automated Low-Altitude Air Delivery*, J. C. Dauer, Ed. Cham: Springer International Publishing, 2022, pp. 159–183.
[11] Kier, T., and Hofstee, J., “VarLoads - Eine Simulationsumgebung zur Lastenberechnung eines voll flexiblen, freifliegenden Flugzeugs,” in *Deutscher Luft- und Raumfahrtkongress*, Dresden, 2004.
[12] Kier, T., Looye, G., Scharpenberg, M., and Reijerkerk, M., “Process, Methods and Tools for Flexible Aircraft Flight Dynamics Model Integration,” in *International Forum on Aeroelasticity and Structural Dynamics*, Stockholm, Sweden, 2007, http://elib.dlr.de/55663/.
[13] Klimmek, T., “Parameterization of topology and geometry for the multidisciplinary optimization of wing structures,” in *CEAS 2009 - European Air and Space Conference*, Manchester, United Kingdom, 2009.
[14] Klimmek, T., Dähne, S., Fröhler, B., Hartmann, J., Kohlgrüber, D., Petsch, M., Schulze, M., Schuster, A., and Süelözgen, Ö., “High-Fidelity-based MDO: A Closer Look at the Selected Sub-Processes Overall Aircraft Design Synthesis, Loads Analysis, and Structural Optimization,” presented at the DLRK 2020 - Deutscher Luft- und Raumfahrtkongress, Virtual event, 2020, https://elib.dlr.de/137392/.
[15] Lin, F., and Hewitt, W. T., “Expressing Coons-Gordon surfaces as nurbs,” *Computer-Aided Design*, vol. 26, no. 2, pp. 145–155, Feb. 1994, https://doi.org/10.1016/0010-4485(94)90035-3.
[16] Liu, D. D., James, D. K., Chen, P. C., and Pototzky, A. S., “Further studies of harmonic gradient method for supersonic aeroelastic applications,” *Journal of Aircraft*, vol. 28, no. 9, pp. 598–605, 1991, https://doi.org/10.2514/3.46070.
[17] Luber, Wolfgang G., Becker, J., and Sensburg, O., “The Impact of Dynamic Loads on the Design of Military Aircraft,” presented at the AGARD Structures and Materials Panel meeting on “Loads and Requirements for Military Aircraft,” Florence, Italy, 1996.
[18] Mancini, A., Zamboni, J., and Moerland, E., “A Knowledge-based Methodology for the Initiation of Military Aircraft Configurations,” presented at the AIAA AVIATION 2021 FORUM, Virtual Event, 2021, https://doi.org/10.2514/6.2021-2789.
[19] Molkenthin, J., “Determination and Verfication of Operational Maneuver Parameters and Time Histories,” presented at the AGARD Structures and Materials Panel meeting on “Loads and Requirements for Military Aircraft,” Florence, Italy, 1996.
[20] Multiple authors, “Design Loads for Future Aircraft,” NATO Research and Technology Organisation, Technical Report RTO-TR-045, Feb. 2002.
[21] Multiple authors, “Loads and Requirements for Military Aircraft,” Florence, Italy, Proceedings of the AGARD Structures and Materials Panel meeting on “Loads and Requirements for Military Aircraft” AGARD Report 815, Feb. 1997.
[22] Neubauer, M., and Gunther, G., “Aircraft Loads,” presented at the RTO AVT Lecture Series on “Aging Aircraft Fleets: Structural and Other Subsystem Aspects,” Sofia, Bulgaria, 2000, https://apps.dtic.mil/sti/citations/ADP010772.
[23] Petiau, C., “Evolution de la philosophie des charges de dimensionnement des avions militaires,” presented at the AGARD Structures and Materials Panel meeting on “Loads and Requirements for Military Aircraft,” Florence, Italy, 1996.
[24] Pratt, K. G., “A revised formula for the calculation of gust loads,” National Advisory Committee for Aeronautics. Langley Aeronautical Lab., Langley Field, VA, Technical Note TN 2964, Jun. 1953, http://ntrs.nasa.gov/search.jsp?R=19930084025.
[25] Pratt, K. G., and Walker, W. G., “A Revised Gust-Load Formula and a Re-evaluation of V-G Data Taken on Civil Transport Airplanes From 1933 to 1950,” National Advisory Committee for

Aeronautics. Langley Aeronautical Lab., Langley Field, VA, Technical Report NACA-TR-1206, 1953.
[26] Probert, B., “Aspects of Wing Design for Transonic and Supersonic Combat Aircraft,” presented at the RTO AVT Course on “Fluid Dynamics Research on Supersonic Aircraft,” Rhode-Saint-Gentèse, Belgium, 1998.
[27] Scharpenberg, M., Kier, T., and Taules, L., “Considerations on an Integral Flight Physics Model with Application to Loads Analysis,” in *SAE International*, 2011, https://doi.org/10.4271/2011-01-2767.
[28] Schulze, M., Klimmek, T., Torrigiani, F., and Wunderlich, T. F., “Aeroelastic Design of the oLAF Reference Aircraft Configuration,” presented at the Deutsche Luft- und Raumfahrtkongress (DLRK) 2021, Bremen (virtuell), 2021, https://elib.dlr.de/143642/.
[29] Schwamborn, D., Gerhold, T., and Heinrich, R., “The DLR Tau-Code: Recent Applications in Research and Industry,” in *European Conference on Computational Fluid Dynamics*, 2006.
[30] Siggel, M., Kleinert, J., Stollenwerk, T., and Maierl, R., “TiGL: An Open Source Computational Geometry Library for Parametric Aircraft Design,” *Math.Comput.Sci.*, vol. 13, no. 3, pp. 367–389, Sep. 2019, https://doi.org/10.1007/s11786-019-00401-y.
[31] Sinha, K., Klimmek, T., Schulze, M., and Handojo, V., “Loads analysis and structural optimization of a high aspect ratio, composite wing aircraft,” *CEAS Aeronaut J*, vol. 12, no. 2, pp. 233–243, Apr. 2021, https://doi.org/10.1007/s13272-021-00494-x.
[32] Stauffer, W. A., Lewolt, J. G., and Hoblit, F. M., “Application of Advanced Methods to Design Loads Determination for the L-1011 Transport,” *Journal of Aircraft*, vol. 10, no. 8, pp. 449–458, 1973, https://doi.org/10.2514/3.60248.
[33] Stauffer, W., Lewolt, J., and Hoblit, F., “Application of advanced methods to the determination of design loads of the Lockheed L-1011 TriStar,” 1972, https://doi.org/10.2514/6.1972-775.
[34] Stradtner, M., Liersch, C. M., and Löchert, P., “Multi-Fidelity Aerodynamic Data Set Generation for Early Aircraft Design Phases,” presented at the AVT-366 Use of Computational Fluid Dynamics for Design and Analysis: Bridging the Gap Between Industry and Developers, 2022.
[35] Struck, H., and Perron, C., “Flight Loads Derived from Operational Maneuvers,” presented at the AGARD Structures and Materials Panel meeting on “Loads and Requirements for Military Aircraft,” Florence, Italy, 1996.
[36] Voß, A., “An Implementation of the Vortex Lattice and the Doublet Lattice Method,” Institut für Aeroelastik, Deutsches Zentrum für Luft- und Raumfahrt, Göttingen, Germany, Technical Report DLR-IB-AE-GO-2020-137, Oktober 2020, https://elib.dlr.de/136536/.
[37] Voß, A., “Design and Structural Optimization of a Flying Wing of Low Aspect Ratio Based on Flight Loads,” Dissertation, Technische Universität Berlin, Berlin, Germany, 2020, https://doi.org/10.14279/depositonce-9858.
[38] Voß, A., “Loads Kernel User Guide,” Institut für Aeroelastik, Deutsches Zentrum für Luft- und Raumfahrt, Göttingen, Germany, Technical Report DLR-IB-AE-GO-2020-136, Jul. 2021, https://elib.dlr.de/140268/.
[39] Voß, A., Handojo, V., Weiser, C., and Niemann, S., “Preparation of Loads and Aeroelastic Analyses of a High Altitude, Long Endurance, Solar Electric Aircraft,” presented at the AEC2020 Aerospace Europe Conference, Bordeaux, France, 2020, https://elib.dlr.de/133496/.
[40] Voß, A., Handojo, V., Weiser, C., and Niemann, S., “Results from Loads and Aeroelastic Analyses of a High Altitude, Long Endurance, Solar Electric Aircraft,” *Journal of Aeroelasticity and Structural Dynamics*, vol. 9, no. 1, pp. 1–22, Jan. 2022, https://elib.dlr.de/147956/.
[41] Watson, G. J., “Eurofighter 2000 Structural Design Criteria and Design Loading Assumptions,” presented at the AGARD Structures and Materials Panel meeting on “Loads and Requirements for Military Aircraft,” Florence, Italy, 1996.
[42] *MIL-A-8860B Airplane Strength and Rigidity General Specifications*. 1987.
[43] *MIL-A-8861B Airplane Strength and Rigidity Flight Loads*. 1986.